Journal of Electronic Materials (2023) 52:6778–6790
https://doi.org/10.1007/s11664-023-10609-1

ORIGINAL RESEARCH ARTICLE

First-Principles Analysis of $CuMg_2InS_4$: Insights into Optical, Piezoelectric, and Thermoelectric Properties

Ouafaa Sadouki[1,2] · Friha Khelfaoui[3] · Fabien Fontaine-Vive[4] · Keltouma Boudia[1,5] · Hayat Hocine[3] · Enis Sert[6] · Ahmed Redha Benrekia[7] · Mama Hamlat[3] · Amel Slamani[8,9] · Fadila Belkharroubi[10] · Kadda Amara[3]

Received: 5 April 2023 / Accepted: 10 July 2023 / Published online: 1 August 2023

Abstract

This study presents a comprehensive investigation of the properties of the compound $CuMg_2InS_4$ chalcogenide using density functional theory (DFT) simulation. The full potential linearized augmented plane wave plus local orbitals method with generalized gradient approximation has been employed to optimize its stannite, kesterite, wurtzite-stannite (WS), and monoclinic phases. The calculations show that $CuMg_2InS_4$ is a direct band gap semiconductor, with a band gap of 1.64 eV in its structural ground phase, which is the WS phase. The study further analyzes the structural, mechanical, electronic, optical, and thermoelectric properties of this phase. By utilizing the modified Becke–Johnson potential (TB-mBJ), $CuMg_2InS_4$ is a thermoelectric material with low thermal conductivity and high power factor. Additionally, the DFT-D3 method shows that the material is dynamically stable and exhibits a piezoelectric behavior. These results provide crucial insights into the characteristics of $CuMg_2InS_4$, which have significant practical applications in various fields, such as energy conversion and electronic devices.

Keywords FP-LAPW · DFT-D3 · stability · semiconductor · thermoelectric properties · piezoelectricity

Introduction

The importance of harvesting solar energy has expanded enormously in response to rising global energy demand and the need for sustainable and renewable resources.[1] To address this growing demand, it is crucial to enhance the efficiency of solar panels in capturing and converting sunlight into usable electrical energy. Thin-film solar cells have emerged as a flexible and economically viable technology for proficiently capturing solar energy. Additionally, the conversion of heat into electrical energy through thermoelectric (TE) power generation offers a promising avenue for utilizing renewable energy sources.[2]

In this context, material science assumes a critical role in the development of advanced materials with superior properties suitable for use in thin-film solar cells and TE power systems. This study aims to contribute to this field by investigating novel quaternary chalcogenide materials and

✉ Friha Khelfaoui
friha.khelfaoui@univ-saida.dz

1 Department of Matter Sciences, Faculty of Sciences and Technology, Tissemsilt University, Bougara, Algeria

2 Laboratoire d'Etude Physique des Matériaux, Universit´e des Sciences et de La Technologie D'Oran Mohamed Boudiaf, USTO-MB, El M'Naouar, BP 1505, 31000 Oran, Algeria

3 Laboratory of Physicochemical Studies, University of Saida-Dr. Moulay Tahar, 20000 Saida, Algeria

4 Institut de Chimie de Nice, Université Côte d'Azur, CNRS UMR 7272, 06108 Nice, France

5 Physical Engineering Laboratory, University of Tiaret, 14000 Tiaret, Algeria

6 Departement of Physics, Faculty of Science, Çankiri Karatekin University, Çankiri, Turkey

7 Yahia Fares university of Medea, Medea, Algeria

8 Laboratory of Physico-chemistry of Advanced Materials, University of Djillali Liabes, BP 89, , 2-2000 Sidi-Bel-Abbes, Algeria

9 Department of Physics, Faculty of Science and Technology, University of Relizane, 48000 Relizane, Algeria

10 Laboratory of Analysis and Aplication of Radiations (LAAR), Faculty of Physics, University of Science and Technology of Oran Mohamed Boudiaf (USTO-MB), 1505 El Menouar, 31000 Oran, Algeria

their properties, with the ultimate objective of enabling cost-effective and efficient utilization of solar energy and heat conversion technologies.

In recent times, quaternary chalcogenides, also known as diamond- like semiconductors, have gained significant attention from researchers. This is due to their diverse range of intriguing features that hold potential for various technological applications such as photovoltaic, nonlinear optics,[3] and solar cells.[4] The theoretical and experimental syntheses of quaternary I_2-II-IV-VI_4 (I = Cu, Ag, II = Zn, Cd, Iv = Si, Ge, Sn, VI = S, Se, Te) compounds began in 1958, when Goodman demonstrated that various series of new semiconductor compounds could be derived from the known ones by a process of 'cross-substitution'. This involves replacing one element per pair of elements from other groups of the periodic table while keeping the valence electron constant.[5] These materials exhibited a notable transition from semiconducting to semimetallic behavior, dependent on the specific phase and chemical compositions.[6]

As an example, the ternary compound $CuGaS_2$ can be produced by substituting one Cu^+ cation and one Ga^{+3} cation for Mg^{+2} cations in the diamond structure of MgS. If the Ga atom in the ternary compound $CuGaS_2$ is replaced by Mg^{+2} and In^{+3} cations, along with one of the Cu atoms being replaced by Mg^{+2}, a quaternary compound $CuMg_2InS_4$ is formed. These compounds can exhibit various space group symmetries and cation ordering methods, including stannite (ST), kesterite (KS), wurtzite-stannite (WS), and monoclinic (Pc) phases.[7] The investigation of quaternary chalcogenide semiconductors has spanned over 40 years; however, the nature of their crystal structures has remained a topic of contention.

One such investigation involved the synthesis of a novel family of quaternary semiconductors, namely Cu_2ZnAS_{4-x} and Cu_2ZnAS_4 (where A = Al, Ga, In), as wurtzite phase nanocrystals using the colloidal hot-injection method. The direct band gap of these materials within the visible wavelength range, coupled with their exceptional absorption cross-section, has generated significant potential for their utilization in solar energy conversion endeavors.[8] In another study, researchers synthesized nanocrystals of the ST phase $CuZn_2AlS_4$ (CZAS) and discovered that, from an energy perspective, the ST structure exhibited greater stability compared to the KS, WS, orthorhombic, and zinc blende structures.[9]

In an additional exploration, the Cu_2MgSnS_4 compound was synthesized using hot injection methods, revealing that it crystallizes in the tetragonal structure (i.e., KS). Furthermore, UV-Vis absorption spectroscopy revealed that the compound possesses an optical gap of 1.63 when synthesized using hot injection methods. Using another syntheses technique called ultrasonic co-sputtering, the same compound was found to have a tetragonal structure with an optical gap of 1.76 eV.[10] In a related theoretical inquiry, Akil et al studied a compound of the same category but with a different structure, Na_2ZnSnS_4 , and found that it is stable in the KS phase. Their findings were in good agreement with experimental data.[11,12]

In this study, to explore the properties of the $CuMg_2InS_4$ chalcogenide, the state-of-the-art ab initio self-consistent FP-LAPW + lo method, coupled with the generalized gradient approximation and Perdew–Burke–Ernzerhof (GGA-PBE) method derived from Perdew's 2008 functional theory, has been employed. To achieve a more precise determination of the band gap energy, the modified Becke–Johnson potential (TB-mBJ) has been utilized to calculate the density of states and band structure.[13] Our investigation primarily focused on evaluating the structural, mechanical, thermodynamic stabilities, linear optical response, and thermoelectricity of the compound. It is noteworthy that we utilized two different codes for computation, namely Wien2k and VASP.

The organization of this paper is as follows: section "Computational Details" outlines the technical aspects of our calculation in a succinct manner. In section "Results and Discussion", we present our key findings and analyze the structural, elastic, thermoelectric, and optical properties of the compound under examination. Lastly, in section "Conclusion", we summarize our main outcomes and present our conclusions in a brief manner.

Computational Details

We employed the FP-LAPW + lo method, as implemented in the Wien2k code,[14] to investigate the structural, electronic, and optical properties of the $CuMg_2InS_4$ compound. To calculate the exchange correlation potential, we used the PBE correlation energy functional, which is widely used in density functional theory (DFT) calculations. However, it is known to underestimate the band gap of semiconductors.[15] Therefore, to obtain a more accurate description of the band gap energy, The TB-mBj potential[13,16–18] is used to calculate the density of states and band structure. In order to ensure accurate results, we performed convergence tests on the parameters R.Kmax and Kpoints. After testing various values, the R.Kmax of 8 and Kpoints of 600 were found to be optimal for our study. The muffin-tin radii (RMTs) for the Cu, Mg, In, and S were set to 2.16, 1.8, 2.3, 1.84, respectively. These parameters were used to accurately describe the structural, electronic, and optical properties of the $CuMg_2InS_4$ compound. It is important to note that the choice of RMTs can significantly affect the results, and, hence, they were carefully selected based on previous studies and theoretical considerations. During the self-consistent cycles, we set the cut-off energy at − 6 Ry, which separates the valence

and core states. The energy and charge convergence criteria were chosen to be 10^{-6} Ry, and 10^{-5} e, respectively.

To investigate the TE transport properties of the $CuMg_2InS_4$ compound, we utilized the FL-APW method with the TB-mBJ exchange potential[19] to ensure accurate results, and a very high- density k-grid of 34 × 34 × 34 k-points was used for integration over the irreducible Brillouin zone. The TE properties versus temperature were then calculated using the BoltzTrap code.[20]

Regarding the calculations performed using the VASP code, it should be noted that all the energy calculations were conducted using VASP 5.4.4,[21,22] which is a DFT- based code. The calculations employed the GGA-PBE[23] for the exchange-correlation energy, as well as recent projector-augmented wave potentials. A plane wave basis set with an energy cutoff of 600 eV and reciprocal space grid interval of 0.25 Å was utilized. In addition, the van der Waals dispersion energy correction was computed using Grimme et al.'s DFT-D3 method.[24,25] Calculations conducted using VASP are often referred to as "parameter-free" since the user is only required to input the atom types and initial coordinates. The choices outlined above primarily concern achieving convergence in the calculations. The crystal structures underwent energy minimization through the optimization of cell parameters and atomic positions, resulting in residual forces less than 0.01 eV/Å and an average residual force nearly one order of magnitude smaller. A series of single-point energy calculations were subsequently performed to calculate the Hellmann–Feynman forces acting on all atoms in the cell. Each structure was obtained by displacing one of the symmetry-inequivalent atoms by 0.01 Å along both positive and negative Cartesian directions. Using these data, the dynamical matrix was constructed and diagonalized for any k-vector using the PHONOPY program.[26] VASP calculates the second-order derivatives of the total energy with respect to ion positions using a finite difference approach. The resulting data is then used to construct and diagonalize the dynamical matrix, from which phonon modes, elastic, internal strain tensors, and piezoelectric constants can be derived. Additionally, linear response theory is employed to calculate the ionic contribution to the dielectric tensor.

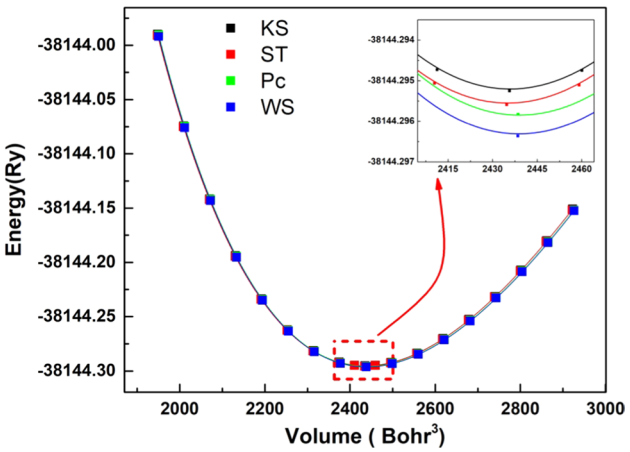

Fig. 1 (Color online) Calculated energy versus volume, using FP-LAPW, for KS, WS, ST, and Pc phases of $CuMg_2InS_4$ compound.

Results and Discussion

Structural Properties and Phase Stability

The quaternary diamond-like semiconductor compounds I_2–II–IV–VI_4 can be synthesized from I–III–VI_2 compounds by substituting every two atoms from the III column with one atom from the II column and one atom from the IV column, resulting in a doubled structure of the I–III–VI_2 compound.[4,7,27] The latter ternary compound is also obtained from a binary II–VI compound by replacing one atom from column II with one atom from column I and one atom from column III.[28,29] Our compound $CuMg_2InS_4$ has three crystal structures: firstly, a tetragonal structure with a KS phase (space group I-4; no.79) and a ST phase (space group I-42 m; no. 121) where $a = b \neq c$ and $\alpha = \beta = \gamma = 90°$; secondly, an orthorhombic structure with a WS phase (space group Pmn21; no.1) where $a \neq b \neq c$ and $= \beta = \gamma = 90°$; and finally, a Pc structure (space group Pc; no.7) where $a \neq b \neq c$, $\alpha = \gamma = 90°$, and $\beta \neq 90°$. A system's overall energy, or more commonly, the difference in energy between distinct phases, can provide valuable insights into its properties. To gain a better understanding of our compound, $CuMg_2InS_4$, we fitted the change in total energy with respect to the volume for its four phases with the Birch–Murnaghan equation of state.[30] Based on our calculations, the energy order of the phases for $CuMg_2InS_4$ is WS < Pc < ST < KS,

Table I Lattice parameters *a* (Å), *b/a*, *c/a*, bulk modulus *B* (in GPa), its derivative *(B')*, and formation energy $E_{formation}$ (in eV/atom) for KS, WS, ST, and Pc phases of the $CuMg_2InS_4$ compound

Phase		*A*	*b/a*	*c/a*		*B*	*B'*	$E_{formation}$
KS	FP-LAPW	5.6415	1	2.0103	β = α = γ = 90°	61.0537	4.5318	−0.9549
ST	FP-LAPW	5.6655	1	1.9843	β = α = γ = 90	60.9166	4.5265	−0.9552
WS	FP-LAPW	8.0185	0.8614	0.8136	β = α = γ = 90	60.7529	4.5281	−0.9558
	DFT-D3	8.0210	0.8609	0.8134				
Pc	FP-LAPW	6,5218	1.0636	1.5809	α = γ = 90°, β = 129.25°	60.9049	4.5367	−0.9555

indicating that the WS phase in the most stable (see Fig. 1). Conversely, the KS structure has the highest total energy, suggesting that it is the least energetically stable. Table I summarizes the lattice constants, equilibrium volume, bulk modulus, and pressure derivative of the WS, Pc, ST, and KS phases of the $CuMg_2InS_4$. and Table II presents the relaxed atomic positions of the atoms in the structural ground phase of the $CuMg_2InS_4$, showing good agreement between the results obtained using the FP-LAPW and DFT-D3 approximations. As there is currently no available experimental or theoretical data with which to compare, our findings can serve as a useful reference for guiding future research on this compound.

Formation energy is a measure of the stability of a crystal phase relative to its constituent elements in their standard states.[31] A lower formation energy indicates greater stability, suggesting that the phase is more likely to occur under given conditions. Based on the calculated formation energies, as shown in Table I, the WS phase has the lowest formation energy, followed by the ST, Pc, and finally KS phases, indicating that WS is the most stable phase while Pc is a less stable one.

Mechanical Properties

Stress tensors were calculated for the WS phase of the $CuMg_2InS_4$ compound to analyze its mechanical stability and determine other mechanical properties. Due to its crystalline symmetry, the number for C_{ij} constants in this phase has been reduced to nine independent elastic constants, namely C_{11}, C_{12}, C_{13}, C_{22}, C_{23}, C_{33}, C_{44}, C_{55}, and C_{66}.[32] Other mechanical properties, such as the bulk modulus (B), shear modulus (G), Young's modulus (E), and Poisson's ratio (v), can be computed using the elastic constant through the Voigt–Reuss–Hill approximation. These properties can be expressed as[33–35]:

$$B_V = \frac{1}{9}(C_{11} + 2C_{12} + 2C_{13} + C_{22} + 2C_{23} + C_{33} \quad (1)$$

$$B_R = \frac{1}{(S_{11} + S_{22} + S_{33}) + 2(S_{12} + S_{13} + S_{23})} \quad (2)$$

$$G_V = \frac{1}{15}(C_{11} - C_{12} - C_{13} + C_{22} - C_{23} + C_{33} + 3C_{44} + 3C_{55} + 3C_{66}) \quad (3)$$

$$G_R = \frac{15}{4(S_{11} + S_{22} + S_{33}) - 4(S_{12} + S_{13} + S_{23}) + 3(S_{44} + S_{55} + S_{66})}$$

where S_{ij} represents the elastic compliance constants, which are the inverse matrix of C_{ij}. The Hill model calculates the shear modulus and bulk modulus as the arithmetic means of the Voigt and Reuss bounds[36,37:]

$$B = \frac{B_V + B_R}{2} \quad (4)$$

$$G = \frac{G_V + G_R}{2} \quad (5)$$

To calculate the values of v and E, the following equations are utilized[38]:

$$E = \frac{9BG}{3B + G} \quad (6)$$

$$v = \frac{3B - 2G}{2(3B + G)} \quad (7)$$

The results obtained from the FL-APW and DFT-D3 methods are presented in Table III. It is evident that the values obtained from the FP-LAPW method closely match those obtained from the DFT-D3 method, thereby

Table II Calculated atomic positions for the structural ground phase (WS phase) of $CuMg_2InS_4$

Method	Atom	Site	*x/a*	*y/b*	*z/c*
FP-LAPW	Mg	4b	0.249594	0.170021	0.500439
	Cu	2a	0.00000	0.669940	0.498110
	In	2a	0.00000	0.333664	0.999889
	S(1)	4b	0.26184	0.169376	0.120807
	S(2)	2a	0.00000	0.346816	0.614914
	S(3)	2a	0.00000	0.670919	0.139693
DFT-D3	Mg	4b	0.249389	0.169712	0.500766
	Cu	2a	0.000000	0.670651	0.497001
	In	2a	0.000000	0.333553	0.999782
	S(1)	4b	0.263558	0.168801	0.121926
	S(2)	2a	0.000000	0.347531	0.612804
	S(3)	2a	0.000000	0.672570	0.139693

Table III Elastic constants C_{ij}, bulk B, Young's E, and shear moduli G (in GPa), and Poisson ratio v for the structural ground state of $CuMg_2InS_4$

Method	Compound	C_{11}	C_{22}	C_{33}	C_{44}	C_{55}	C_{66}	C_{12}	C_{13}	C_{23}	*B*	*E*	*G*	*v*
FP-LAPW	$CuMg_2InS_4$	91.99	122.58	101.55	19.42	18.45	28.34	47.30	40.52	56.30	66.14	64.57	24.15	0.34
	Na_2ZnSnS_4:KS[11]										41.71	27.90	10.05	
	Cu_2MgSnS_4:ST[41]										73.85	68.72	25.55	
DFT-D3	$CuMg_2InS_4$	96.44	93.74	108.07	21.533	19.26	21.85	48.14	42.08	39.98	62.04	54.03	19.94	0.35

indicating the reliability of our calculations. Furthermore, all of the calculated elastic constants are positive, and they satisfy all mechanical stability criteria[39,40]:

$$C_{11} > 0; C_{11}C_{22} > C_{12}^2$$
$$C_{11}C_{22}C_{33} + 2C_{12}C_{13}C_{23} - C_{11}C_{23}^2 - C_{22}C_{13}^2 - C_{33}C_{12}^2 > 0$$
$$C_{44} > 0; C_{55} > 0; C_{66} > 0 \quad (8)$$

The calculated bulk modulus (B) of $CuMg_2InS_4$ is less than 100 GPa, indicating that it can be categorized as a soft material. When comparing this compound with Cu_2MgSnS_4[41] and Na_2ZnSnS_4,[11] it is found that Cu2Mg-SnS4 has the highest bulk, and shear moduli, followed by $CuMg_2InS_4$, and then Na_2ZnSnS_4. Thus, Cu_2MgSnS_4 is anticipated to be the stiffest among the three compounds. Moreover, the bulk modulus value is greater than the shear modulus G, indicating that the mechanical stability of this material is more dependent on the G parameter.[42] Furthermore, the B/G ratio confirms that $CuMg_2InS_4$ is ductile ($B/G = 1.75$). The Young's modulus E represents the ratio of linear stress to linear strain, and its value for the $CuMg_2InS_4$ compound is approximately 64 GPa, demonstrating its stiffness properties.

In Fig. 2, the phonon dispersion curve for our material in its structural ground state is presented. The curve was computed using the pseudo-potential, plane wave methods, and finite difference approach[43,44] with GGA, and it is drawn along high symmetry directions within the irreducible Brillouin zone. The positive phonon frequencies in the curve demonstrate the dynamical stability of the material.

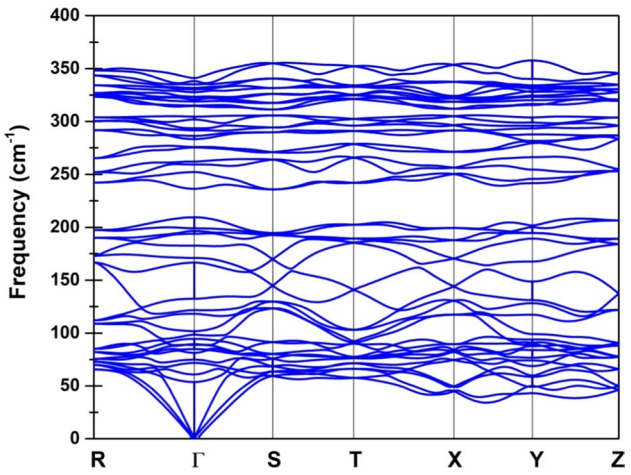

Fig. 2 Phonon dispersion along the principal high-symmetry directions in the Brillouin zone of $CuMg_2InS_4$.

Electronic Properties

Semiconductors are known to have a natural band gap between their valence and conduction bands, making them useful in a variety of applications. Figure 3 displays the band structures of $CuMg_2InS_4$ in WS phase at its equilibrium structural lattice parameters, shown along high symmetry directions in the first Brillouin zone. The use of the GGA approximation indicates that $CuMg_2InS_4$ has a direct band gap of 1.229 eV at the Γ point. Meanwhile, the TB-mBJ calculation demonstrates that WS has a corrected band gap of 1.672 eV.

The electronic states that comprise the estimated energy bands of $CuMg_2InS_4$ can be observed from the corresponding total density of states and partial density of states in an energy range of − 8 eV to 8 eV, as shown in Fig. 4. The valence band (VB) is composed of three distinct regions, labeled VB1, VB2, and VB3, which are situated in different energy ranges. The lowest energy region, VB1, exists between − 6 eV and − 5.5 eV, and is comprised of hybridized S-p and In-s states. The S-p states are mainly responsible for the group of valence bands (VB2) which exist between − 4.8 eV and − 2.3 eV. Finally, the highest energy bands (VB3), ranging from − 0.99 to 0 eV, are dominated by Cu-d and S-p states. The forbidden band widths between VB1 and VB2 and between VB2 and VB3 are found to be 0.66 eV and 0.85 eV, respectively. The conduction band (CB) can be divided into two distinct regions, with a forbidden band width of 0.46 eV. In the lower region of the conduction band (CB1) ranging from 1.80 eV to 2.61 eV, the contribution from In-S states is significant, whereas, in the higher energy region (CB2) from 3.1 eV and above, the contribution from In-p states is dominant.

The highest VB can be mainly attributed to the anti-bonding component of the p-d hybridization between the anion S and the cation Cu, while the lowest CB is primarily dominated by the anti-bonding component of the s-p hybridization between the cation In and anion S. To deepen our comprehension of these bonds, we have conducted a thorough analysis of the electron localization function (ELF) along the plane (001). This comprehensive investigation aims to provide valuable insights into the nature and characteristics of chemical bonding.[45] In Fig. 5, it is evident that there exists an observable antibonding interaction between the sulfur (S) atom (depicted in yellow) and the copper (Cu) atom (depicted in blue). Likewise, a bonding interaction is also present between the indium (In) atom (depicted in purple) and the sulfur (S) atom.

Optical Properties

Dielectric Function

To explain the linear response of a system to electromagnetic radiation, which is related to photon–electron interactions,[46]

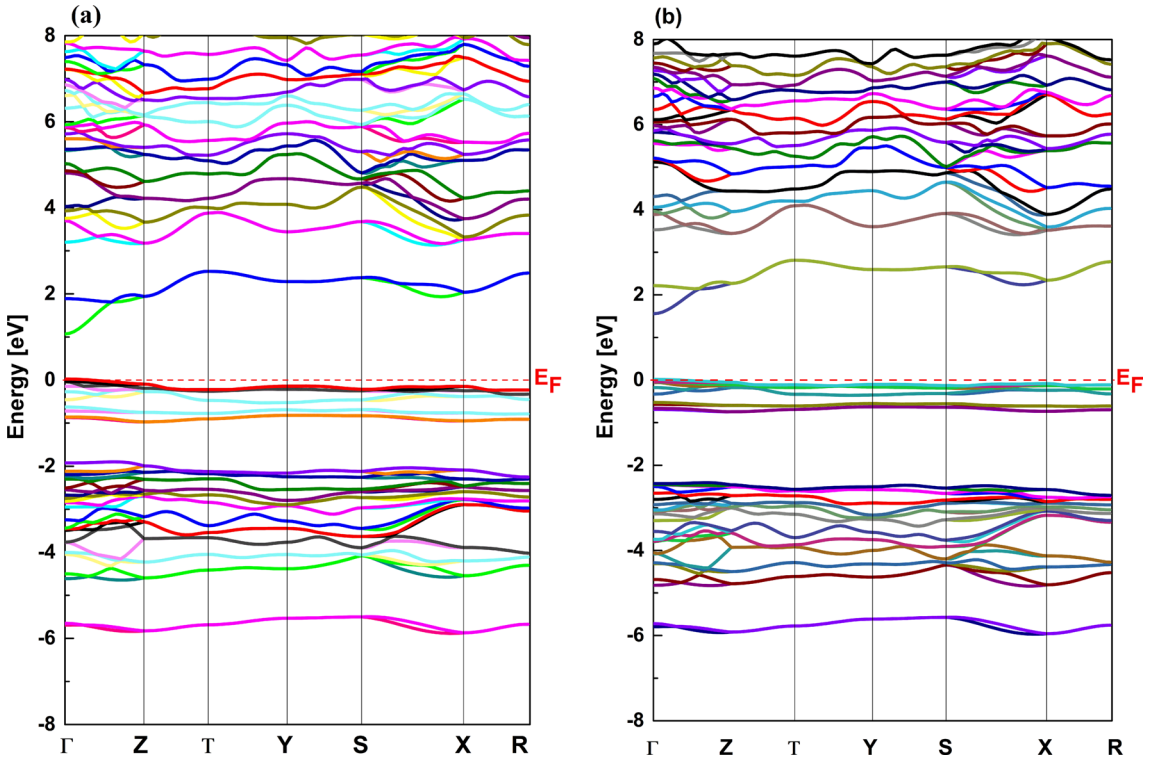

Fig. 3 (Color online) Calculated band structures, along the principal high-symmetry directions in the first Brillouin zone of the WS phase for the $CuMg_2InS_4$ compound, by (a) GGA, and (b) GGA + mBJ approximations.

a complex dielectric function can be defined as a three-dimensional tensor:

$$\varepsilon^{\alpha\beta}(\omega) = \varepsilon_1^{\alpha\beta}(\omega) + i\varepsilon_2^{\alpha\beta}(\omega) \tag{9}$$

Two types of contributions to $\varepsilon^{\alpha\beta}(\omega)$ are intra-band and inter-band transitions. Intra-band transitions are only relevant for metals, while inter-band transitions can be further divided into direct and indirect transitions. The imaginary part of the dielectric function $\varepsilon_2(\omega)$, is determined using momentum matrix elements between the occupied and unoccupied states for inter-band transitions.[3,7]:

$$\varepsilon_2(\omega) = \frac{Ve^2}{2\pi\hbar m^2\omega^2}\int d^3k \sum_{nn'} \left|\langle kn|p|kn'\rangle\right|^2 f_{kn}\left(1-f_{kn'}\right)\delta(E_{kn}-E_{kn'}-\hbar\omega) \tag{10}$$

where $e, V, |kn>, f_{kn,}, \hbar\omega$ and m are the electronic charge, unit cell volume, momentum operator k, crystal wave function n, Fermi distribution function, energy of the incident photon, and electron mass, respectively. This equation considers both intra-band and inter-band transitions, with the latter divided into direct and indirect transitions. The momentum matrix elements between the occupied and unoccupied states are used to determine the imaginary part of the dielectric function. To determine the real part $\varepsilon_1(\omega)$, the Kramers–Kronig relationship can be used[4]:

$$\varepsilon_1(\omega) = 1 + \frac{2}{\pi}M\int_0^{+\infty}\frac{\varepsilon_2(\omega)}{\omega^2}d\omega \tag{11}$$

where M is the integral's principal value. Once the complex dielectric function is established, all other frequency-dependent optical constants can be obtained. Notable optical functions such as reflectivity $R(\omega)$, absorption coefficient $\alpha(\omega)$, refractive index $n(\omega)$, and extinction coefficient $K(\omega)$ are expressed by:

$$\alpha(\omega) = \sqrt{2}\omega\left[\sqrt{\varepsilon_1(\omega)^2+\varepsilon_2(\omega)^2}-\varepsilon_1(\omega)\right] \tag{12}$$

$$R(\omega) = \left|\frac{\sqrt{\varepsilon_1(\omega)+i\varepsilon_2(\omega)}-1}{\sqrt{\varepsilon_1(\omega)+i\varepsilon_2(\omega)}+1}\right|^2 \tag{13}$$

$$n(\omega) = (1/\sqrt{2})\left[\sqrt{\varepsilon_1(\omega)^2+\varepsilon_2(\omega)^2}+\varepsilon_1(\omega)\right]^{\frac{1}{2}} \tag{14}$$

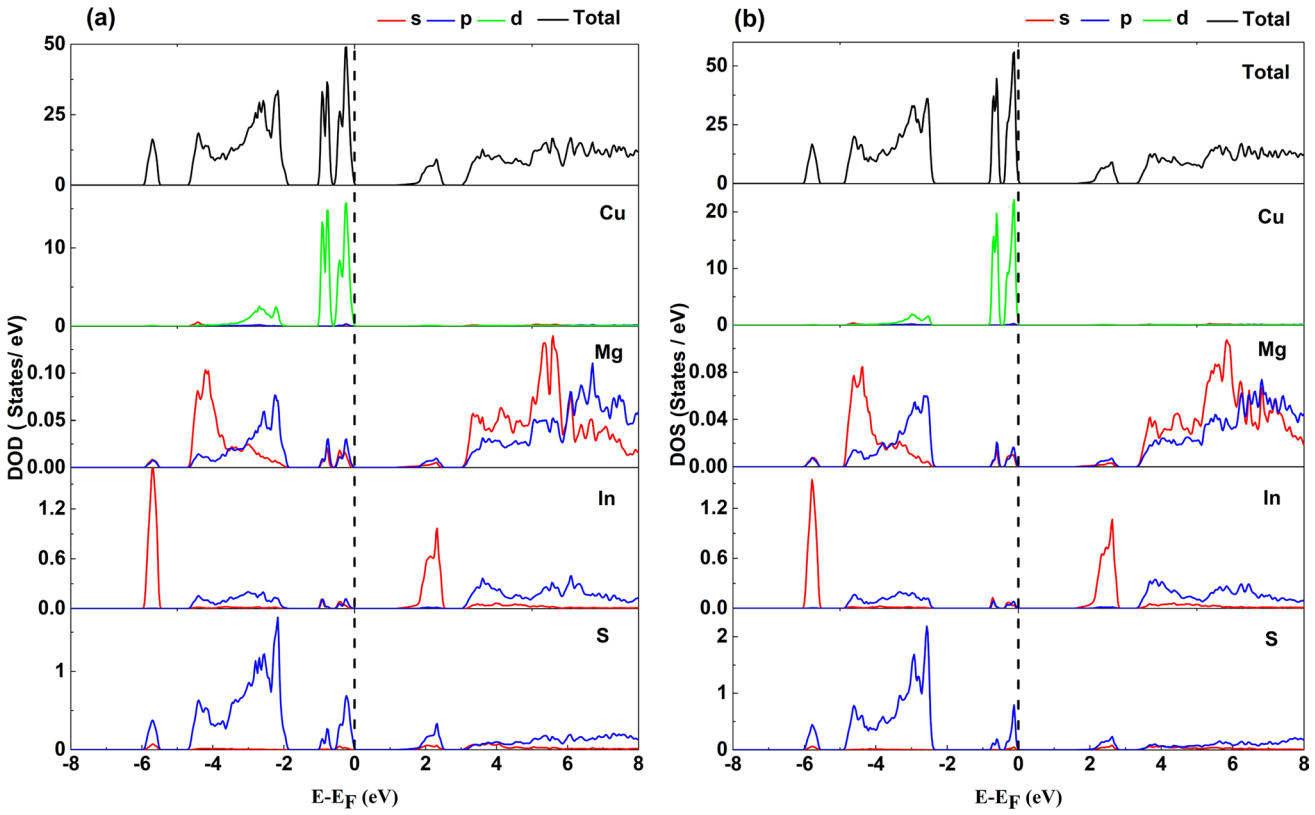

Fig. 4 (Color online) Calculated total and partial densities of states for the WS phase of the $CuMg_2InS_4$ compound, by (a) GGA, and (b) GGA + mBJ approximations.

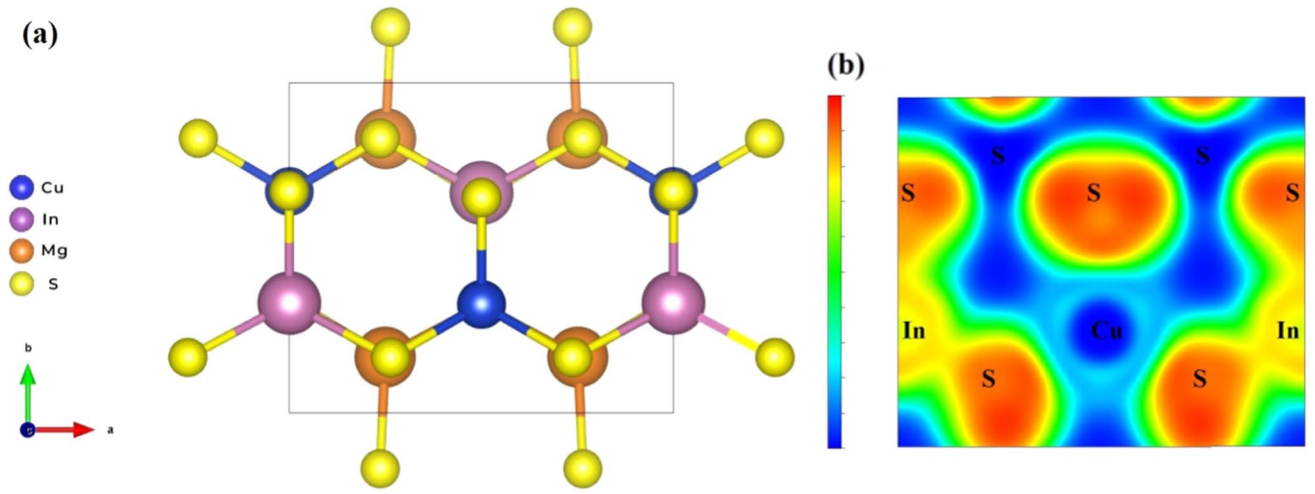

Fig. 5 (a) Atomic structure and (b) ELF analysis in the plane (001).

$$K(\omega) = (1/\sqrt{2})\left[\sqrt{\varepsilon_1(\omega)^2 + \varepsilon_2(\omega)^2} - \varepsilon_1(\omega)\right]^{\frac{1}{2}} \quad (15)$$

This study is focused exclusively on the WS phase, as it is the most stable phase among the ones studied and has a direct band gap. Due to its crystal symmetry, the optical parameter tensors in an orthorhombic structure have three components.

Our analysis, presented in Fig. 6, involved estimating both the imaginary ε_2 and real ε_1 components of the dielectric tensor in different directions. We observed that the lattice constants b and c, which correspond to the y and z directions, respectively, are almost equal. Consequently, the dielectric tensor components along these directions are also similar. However, we noted a clear anisotropy between the x direction and the y and z directions, with a value of approximately 1.62, as shown in Fig. 6. The analysis of the imaginary component ε_2 of the dielectric tensor revealed that the onset of the ε_2 spectra, which corresponds to the first optical critical points, occurs at 1.11 eV. This value is in good agreement with the fundamental energy gap, indicating the optical transition from the highest valence band state to the lowest conduction band state at Γ. We also observed that the optical spectrum ε_2 of the $CuMg_2InS_4$ compound can be divided into three regions, A, B, and C, these regions displaying three main peaks, along with smaller peaks on their right sides. Furthermore, the peak maximums are located within the energy range of 2–7 eV, with the highest peak maximum observed at around 6.24 eV.

By analyzing the highest VB and lowest CB of the $CuMg_2InS_4$ compound, we can connect the trend observed in the imaginary dielectric function with the density of states and band structure. This allows us to identify the origin of the various inter-band transitions that contribute to the observed peaks in the density of states spectra. Specifically, the peaks in region A can be attributed to the transition from S-p and In-s states of VB1 to the In-s state of CB1, while the peaks in region B arise from the transition between S-p states of VB2 and the Mg-p state of CB2. Finally, the peaks in region C result from the transition between Cu-d and S-p states of VB3 and the Mg-p state of CB2.

In the real part spectrum, we observed major peaks with magnitudes of 9.29, 8.20, and 8.62 for ε_1^{xx}, ε_1^{yy}, and ε_1^{zz}, respectively. These peaks are located at energy values of approximately 2.00 eV, 1.97 eV, and 3.63 eV, respectively. Notably, the ε_1^{yy} spectra crosses the zero line four times, whereas both ε_1^{xx} and ε_1^{zz} cross it two times. This feature is prerequisite for the occurrence of plasma oscillations, but it is not a sufficient condition. Therefore, we need to examine the electron energy-loss function $L(\omega)$ to determine the associated screened plasma frequencies.[47] It is worth noting that the quantity ε_1 represents the dispersion, and its transition to zero indicates a lack of diffusion, leading to maximum absorption.[11] Consequently, the analysis of the absorption coefficient can be used to confirm this.

Absorption Coefficient

One of the most significant coefficients in optical properties is the optical absorption coefficient (α), which measures the amount of energy that an electromagnetic wave loses per unit length when it passes through a medium.[48] Figure 7 shows the energy-dependent absorption spectra of $CuMg_2InS_4$ up to 27 eV for each polarization direction. The highest absorption points are at 10.78 eV, 10.54 eV, and 8.58 eV for α^{xx}, α^{yy}, and α^{zz}, respectively, coinciding with a sudden drop in ε_2.

We notice that the absorption is maximum in the ultraviolet range, while the recent study of Cu_2MgSnS_4[41] coumpound reveals that it exhibits a high absorption coefficient in the visible light range.

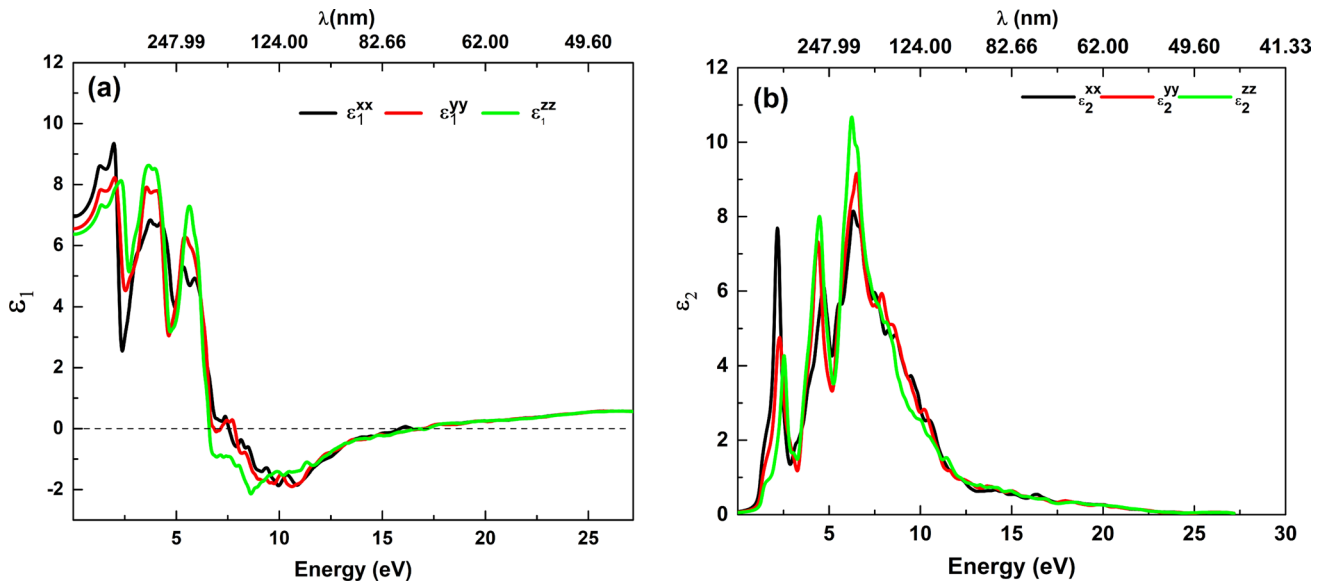

Fig. 6 (Color online) Dielectric response of $CuMg_2InS_4$ in WS phase: energy-dependent variation of its (a) real and (b) imaginary components.

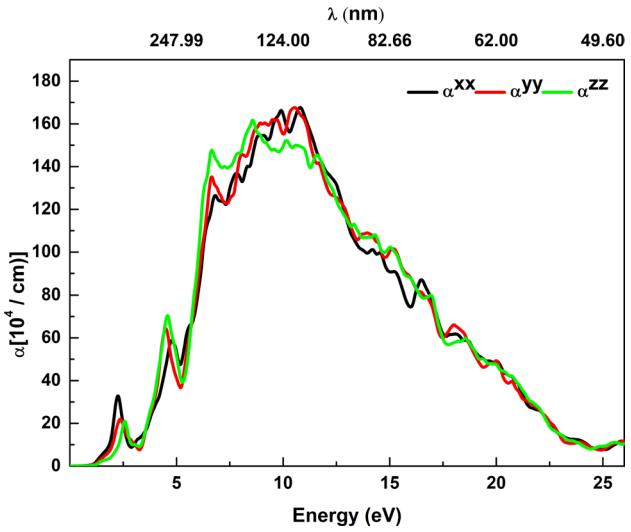

Fig. 7 (Color online) Absorption coefficient for CuMg2InS4 in its WS phase.

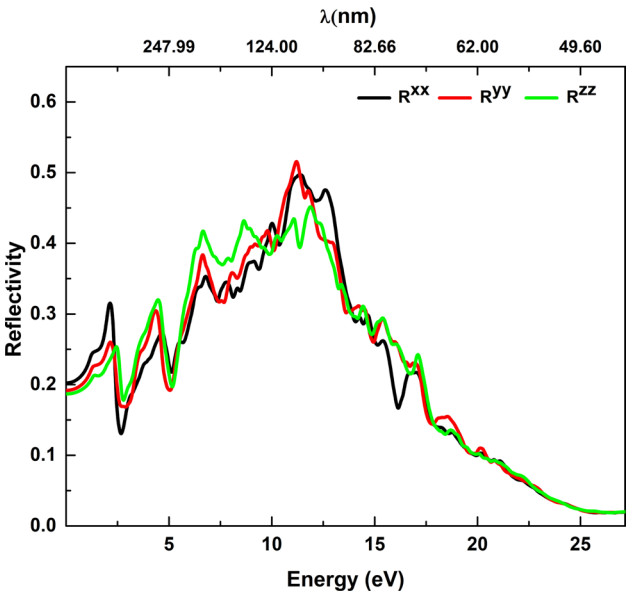

Fig. 8 (Color online) Optical reflectivity for CuMg2InS4 in its WS phase.

Reflectivity

The optical reflectivity, R, represents the proportion of incident power to reflected power. Figure 8 displays the energy-dependent reflectivity of the $CuMg_2InS_4$ compound along crystallographic orientations up to 27 eV. Within the energy range of [0, 11 eV], the reflectivity increases with energy and shows almost identical peaks as the ε_2 curve. The reflectivity reaches its maximum value along each direction between 8 and 15 eV, while the corresponding ε_1 remains below zero, indicating a regime dominated by absorption.

Refractive Index

Figure 9 displays the energy-dependent refractive index n for the three polarizations of $CuMg_2InS_4$ in a spectral range of up to 27 eV. The refractive index exhibits remarkable anisotropy, and both components, n^{yy} and n^{zz}, follow a similar pattern in relation to the hypothetical dielectric constant n, with identical primary peak positions. In the visible and infrared spectrum, n increases with energy. The maximal refractive indices of 3.15, 2.94, and 3.0 are observed at 2.02 eV, 4.14 eV, and 4.06 eV, respectively, for n^{xx}, n^{yy} and n^{zz}. In the ultraviolet region, n decreases significantly after these peaks and reaches its minimum value of 0.36 at 12.77 eV.

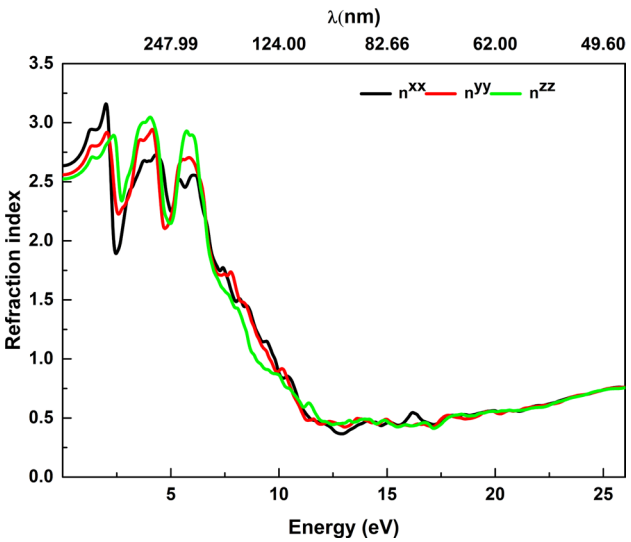

Fig. 9 (Color online) Refractive index for $CuMg_2InS_4$ in itsWS phase.

Thermoelectric Properties

Thermoelectric energy conversion presents a practical solution to address energy challenges, as it enables direct conversion of waste heat energy into electrical energy. At present, research efforts are focused on developing high-performance thermoelectric materials. The performance of these materials is topically evaluated using dimensionless figure-of merit (ZT)[49]:

$$ZT = \frac{S^2\sigma}{\kappa_e + \kappa_L} T \tag{16}$$

where S, σ denote the Seebeck coefficient and electrical conductivity, respectively, and their product $S^2\sigma$ is called the power factor. Additionally,κ_L, κ_e , and T represent lattice thermal conductivity, electronic thermal conductivity, and absolute temperature, respectively. Therefore, achieving a high ZT value requires a high absolute value of the Seebeck

coefficient, along with low thermal conductivity and electrical resistivity. The complex interdependence between these coefficients makes it challenging to provide straightforward design guidelines for optimizing thermoelectric materials. Singh raised this issue at the onset of the current century.[50]

Chalcogenides offer several advantages for use in thermoelectric energy converter applications. Firstly, most of them can be easily doped into *p*- or *n*-type, which is crucial for constructing thermoelectric devices.[51] Secondly, they consist of soft chemical bonds and heavy components, leading to low thermal conductivity.[52] Thirdly, they possess a wide range of structures, which make them suitable for modifying thermoelectric performance. In our study, for instance, they exhibit three distinct crystal forms at room temperature and pressure (tetragonal, orthorhombic, and monoclinic). The temperature-dependent transport properties, estimated using GGA PBE + mBJ potential, are plotted in Fig. 10. The Seebeck coefficient depends not only on temperature but also on the effective mass and concentration of the carrier.[53]

Figure 10a shows that the Seebeck coefficient initially increases rapidly up to 295 K, but then decreases as the temperature rises and the carrier concentration increases, leading to an increase in electrical conductivity and electronic thermal conductivity. The electrical conductivity, illustrated in Fig. 10b, also increases with temperature, indicating semiconductor behavior of our compound. Figure 10c presents the calculated power factor ($P_F = S^2\sigma/\tau$), which reaches a maximum value of 6.10^{10}W/mK^{2}s at temperatures above 400 K. Electronic thermal conductivity (κ_e/τ) , which is directly linked to electrical conductivity, increases relatively linearly with temperature, as shown in Fig. 10d. $CuMg_2InS_4$ compound, similar to $Cu_2ZnSnSe_4$ compound,[54] exhibits a combination of high electrical conductivity and low thermal conductivity, making it a desirable material for efficient thermoelectric conversion. The high electrical conductivity allows for the efficient movement of charge carriers, enabling the generation of an electric current when subjected to a temperature gradient. In layered structural materials, the phonons are dispersed across the layers, resulting in reduced thermal conductivity. As $CuMg_2InS_4$ with a band gap of 1.64 eV exhibits thermoelectric properties, band gap engineering could be interesting in reducing the band deviation and improving thermoelectric performance within the doped system. Hence, our findings are expected to inspire experimentalists to adjust properties through band gap engineering.

Piezoelectricity and Macroscopic Static Dielectric Tensor Ionic Contribution

Piezoelectricity is the ability of material to generate an electrical charge in response to an applied mechanical stress, or to generate a mechanical deformation in response to an applied electric field. The piezoelectric response is dependent on the crystal structure of the material, and chalcogenides are particularly interesting because they can exhibit piezoelectricity despite having a non-centrosymmetric crystal structure.

One example of chalcogenide with piezoelectric properties is the binary compound Bi_2Se_3 which has a layered crystal structure and exhibits strong piezoelectricity along the *c*-axis. This material had been investigated for its potential applications in energy harvesting and sensing.[10] Other chalcogenides, such as binary chalcogenides like MoS_2 and WS2 and WS, have also been shown to exhibit piezoelectricity, although the magnitude of the effect may be weaker. These materials are of interest for applications such as sensors, actuators, and energy-harvesting devices.[29]

Overall, the study of piezoelectricity in chalcogenides in an active area of research, and further exploration of these materials could lead to the development of new technologies and devices. Our compound $CuMg_2InS_4$ belongs to the mm2 class and exhibits five nonzero components, namely e_{15}, e_{24}, e_{31}, e_{32}, and e_{33}as presented in Table IV

These values represent the material's ability to generate an electrical charge in response to mechanical stress or strain in different directions. The values of e_{15}, e_{24}, and e_{31} are relatively high, indicating a strong piezoelectric response in these directions. The magnitude of the e_{32} coefficient is also significant, though slightly lower than the other three coefficients. The value of e_{33} is negative and relatively large, which suggests that the electrical charge generated is in the opposite direction to the applied mechanical stress. The values of the coefficients depend on the crystal structure and composition of the material. The obtained values of the piezoelectric coefficients, e_{15}, e_{24}, and e_{31}, suggest that the studied compound shares similar piezoelectric properties to Cu_2ZnSnS_4 . Both compounds possess a non-centrosymmetric structure, which enables the generation of piezoelectricity in the same directions. This similarity in their piezoelectric properties underscores the potential for these materials to be utilized in analogous applications requiring strong and effective piezoelectric behavior.[55] Overall, the obtained values of the piezoelectric coefficient suggest that $CuMg_2InS_4$ has a strong and complex piezoelectric response that could make it suitable for a range of different applications. However, the suitability of the material will depend on factors such as its mechanical and thermal properties, as well as the specific requirements of the application.

The macroscopic static dielectric tensor describes the response of material to an external electric field, and it can be decomposed into electronic and ionic contribution. The ionic contribution to the macroscopic static dielectric tensor (ϵ) is related to the polarization of the ions in the crystal lattice. The calculated ε,, using DFT-D3 method, is

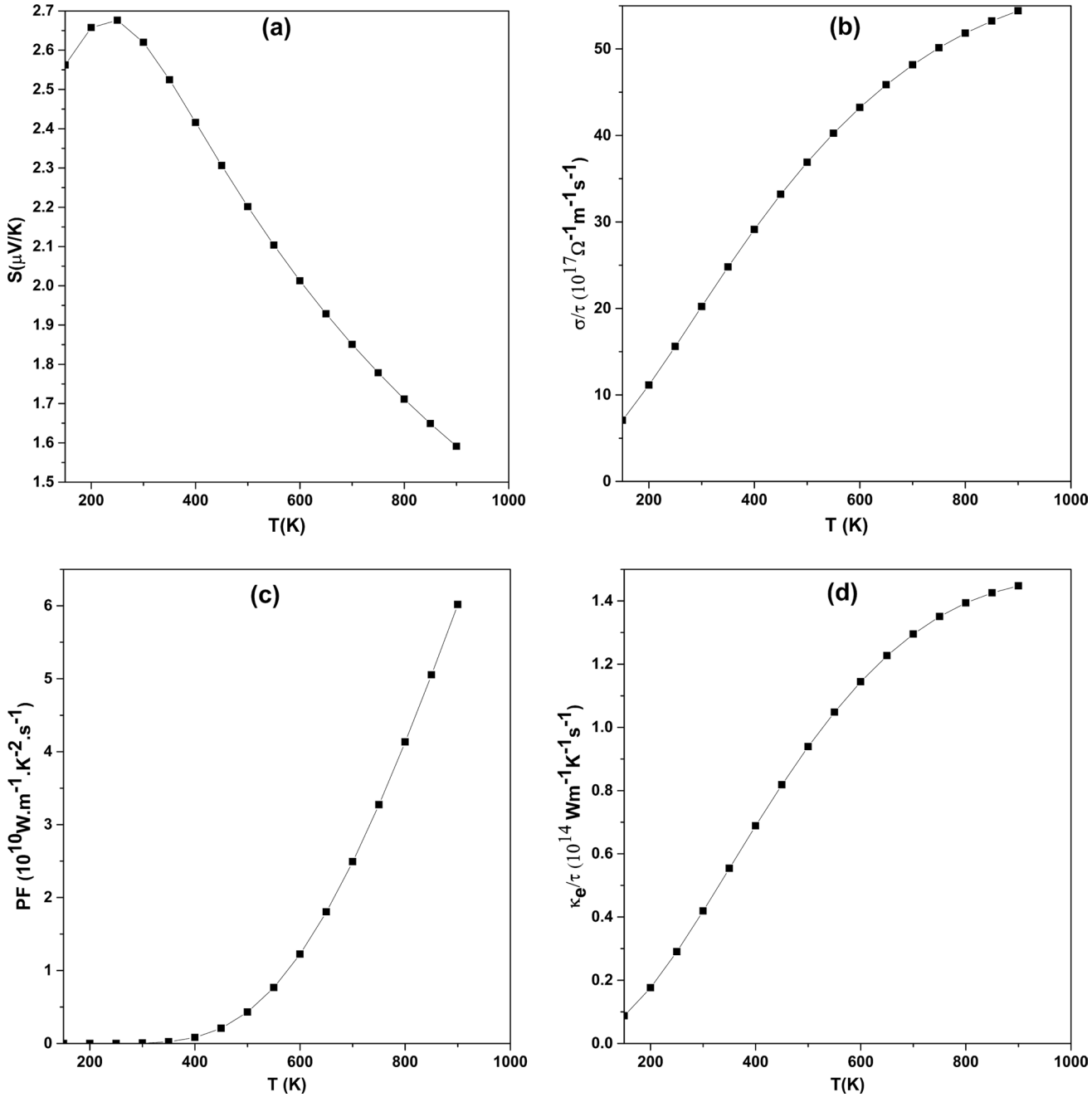

Fig. 10 Temperature-dependent transport properties for $CuMg_2InS_4$ in the WS phase: (a) Seebeck coefficient (S), (b) electrical conductivity, (c) power factor, and (d) electronic thermal conductivity.

Table IV Calculated piezoelectric coefficients e_{ij} (C/m^2)

Piezoelectric coefficient (*dij*)	e_{15}	e_{24}	e_{31}	e_{32}	e_{33}
Calculated value	0.42621	0.43672	0.53291	0.43272	−0.92777

$$\epsilon = \begin{pmatrix} 2.486342 & -0.192619 & -0.152069 \\ -0.192619 & 3.110964 & 0.221177 \\ -0.152069 & 0.221177 & 3.196729 \end{pmatrix} \quad (17)$$

The obtained output gives the ionic contribution to the macroscopic static dielectric tensor. The tensor is a 3 × 3 matrix with elements given in units of F/m, and it describes how the electric field interacts with the ions in the crystal lattice.

The diagonal elements of 2.786342, 3.110964, and 3.196729 correspond to the polarizability of the lattice along the *x, y*, and **z** directions, respectively. The off-diagonal elements (− 0.192619, 0.221177, and − 0.152069) correspond to the correlation between the polarizability in different directions. Therefore, these values describe the ionic contribution to the macroscopic static dielectric tensor for $CuMg_2InS_4$.

Conclusions

We have presented a comprehension theoretical investigation of the structural, electrical, optical, and thermoelectric properties of $CuMg_2InS_4$ within the GGA approximation in the framework of DFT. Our results show that the WS phase is the most energetically and mechanically stable phase of the investigated chalcogenide. The computed band structure and density of states by GGA + TB-mBJ approximation demonstrate that the compound is a direct band gap semiconductor with a band gap of approximately 1.64 eV. The linear optical properties, including the complex dielectric function, refractive index, absorption coefficient, and reflective coefficient, were also analyzed. We found that the TB-mBJ method is more reliable for optical property calculations, and our calculations show that the compound has high absorption, high reflection, and high refraction at different energy levels, indicating its suitability for various optical applications. Regarding the thermoelectric properties, $CuMg_2InS_4$ has a low thermal conductivity and a high power factor, making it suitable for thermoelectric applications. Additionally, the results on its piezoelectric coefficients suggest that the material can produce an electric charge when subjected to mechanical stress or strain in various directions. These findings provide a foundation for future experimental investigation of the properties of $CuMg_2InS_4$ and its potential applications in various fields.

Acknowledgments This work was supported by the French government, through the UCAJEDI investments in the future project managed by the National Research Agency (ANR) under reference number ANR-15-IDEX-01. The authors are grateful to the OPAL infrastructure and the University of coté d'Azur's Center for High-performance computing for providing resources and support.

Conflict of interest The authors declare that they have no known competing financial interests or personal relationships that could have appeared to influence the work reported in this paper.

References

1. I. El Radaf, Structural, Optical, Electrical, and Photovoltaic Investigations of p-Type $Cu_2MnSnSe_4$ Thin Films as a Novel Absorber Layer for Thin Film Solar Cells. *Appl. Phys. A* 129, 1 (2023).
2. D. Behera and S.K. Mukherjee, First-Principles Calculations to Investigate Structural, Optoelectronics and Thermoelectric Properties of Lead Free Cs_2GeSnX_6 (X = Cl, Br). *Mater. Sci. Eng., B* 292, 116421 (2023).
3. S. Levcenco, D. Dumcenco, Y. Huang, E. Arushanov, V. Tezlevan, K.-K. Tiong, and C. Du, Polarization-Dependent Electrolyte Electroreflectance Study of Cu_2ZnSiS_4 and $Cu_2ZnSiSe_4$ Single Crystals. *J. Alloy. Compd.* 509, 7105 (2011).
4. C.M. Fella, Y.E. Romanyuk, and A.N. Tiwari, Technological Status of $Cu_2ZnSn(S, Se_)4$ Thin Film Solar Cells. *Sol. Energy Mater. Sol. Cells* 119, 276 (2013).
5. C. Goodman, The Prediction of Semiconducting Properties in Inorganic Compounds. *J. Phys. Chem. Solids* 6, 305 (1958).
6. W. Shi, A.R. Khabibullin, and L.M. Woods, Exploring Phase Stability and Properties of $I–II_2–III–VI_4$ Quaternary Chalcogenides. *Adv. Theory Simul.* 3, 2000041 (2020).
7. S. Chen, X. Gong, A. Walsh, and S.-H. Wei, Electronic Structure and Stability of Quaternary Chalcogenide Semiconductors Derived from Cation Cross-Substitution of II–VI and $I–III–VI_2$ Compounds. *Phys. Rev. B* 79, 165211 (2009).
8. A. Ghosh, S. Palchoudhury, R. Thangavel, Z. Zhou, N. Naghibolashrafi, K. Ramasamy, and A. Gupta, A New Family of Wurtzite-Phase Cu_2ZnAS_{4-x} and $CuZn_2AS_4$ (A = Al, Ga, In) Nanocrystals for Solar Energy Conversion Applications. *Chem. Commun.* 52, 264 (2016).
9. A. Ghosh, R. Thangavel, and A. Gupta, Chemical Synthesis, Characterization and Theoretical Investigations of Stannite Phase $CuZn_2AlS_4$ Nanocrystals. *New J. Chem.* 40, 1149 (2016).
10. M. Wei, Q. Du, R. Wang, G. Jiang, W. Liu, and C. Zhu, Synthesis of New Earth-Abundant Kesterite Cu_2MgSnS_4 Nanoparticles by Hot-Injection Method. *Chem. Lett.* 43, 1149 (2014).
11. Z. Akil, M. Zemouli, H. Boutaleb, K. Amara, F. Khelfaoui, and M. Elkeurti, First-Principles Study of Structural, Dynamical, Elastic, Electronic, Optical, and Thermodynamic Properties of Na_2ZnSnS_4 Compound. *Can. J. Phys.* 100, 405 (2022).
12. J. He, Y. Guo, W. Huang, X. Zhang, J. Yao, T. Zhai, and F. Huang, Synthesis, Crystal Structure, and Optical Properties of Noncentrosymmetric Na_2ZnSnS_4. *Inorg. Chem.* 57, 9918 (2018).
13. D. Koller, F. Tran, and P. Blaha, Improving the Modified Becke–Johnson Exchange Potential. *Phys. Rev. B* 85, 155109 (2012).
14. P. Blaha, K. Schwarz, G. K. Madsen, D. Kvasnicka, J. Luitz, An augmented plane wave+ local orbitals program for calculating crystal properties **60**, 1 (2001).
15. Á. Morales-García, R. Valero, and F. Illas, An Empirical, yet Practical Way To Predict the Band Gap in Solids by Using Density Functional Band Structure Calculations. *The Journal of Physical Chemistry C.* 121, 18862 (2017).
16. A. Maizia, F. Belkharroubi, M. Bourdim, F. Khelfaoui, S. Azzi, and K. Amara, First-principles Study of a Half-metallic Ferrimagnetic New Full-Heusler Mn_2OsGe Alloy. *Spin.* 10(4), 2050026 (2020).
17. M. Bouhbou, R. Moubah, K. Bakkari, H. Zaari, A. Sabrallah, F. Khelfaoui, N. Mliki, M. Abid, A. Belayachi, and H.M. Lassri, Half-Metallicity and Electronic Studies of $Cd_{1-x}ZnxCr_2Se_4$ Chromium Selenospinels. *J. Magn. Magn. Mater.* 476, 86 (2019).
18. L. Drici, F. Belkharroubi, F.Z. Boufadi, I. Ameri, M. Ameri, W. Belkilali, S. Azzi, F. Khelfaoui, and Y. Al-Douri, First-Principles Calculations of Structural, Elastic, Electronic, and Optical Properties of CaYP (Y = Cu, Ag) Heusler Alloys. *Emerg. Mater.* 5, 1039 (2022).
19. F. Tran and P. Blaha, Accurate Band Gaps of Semiconductors and Insulators with a Semilocal Exchange-Correlation Potential. *Phys. Rev. Lett.* 102, 226401 (2009).
20. G.K. Madsen and D.J. Singh, BoltzTraP: A code for calculating band-structure dependent quantities. *Comput. Phys. Commun.* 175, 67 (2006).

21. S. J. Clark, M. D. Segall, C. J. Pickard, P. J. Hasnip, M. I. Probert, K. Refson, M. C. Payne, First principles methods using CASTEP. Zeitschrift für kristallographie-crystalline materials. **220**, 567 (2005).
22. G. Sun, J. Kürti, P. Rajczy, M. Kertesz, J. Hafner, and G. Kresse, Performance of the Vienna ab Initio Simulation Package (VASP) in Chemical Applications. *J. Mol. Struct. (Thoechem)* 624, 37 (2003).
23. J.P. Perdew, W. Yang, K. Burke, Z. Yang, E.K. Gross, and M. Scheffler, Understanding Band Gaps of Solids in Generalized Kohn-Sham Theory. *Proc. Natl. Acad. Sci.* 114, 2801 (2017).
24. S. Grimme, J. Antony, S. Ehrlich, and H. Krieg, A consistent and Accurate ab Initio Parametrization of Density Functional Dispersion Correction (DFT-D) for the 94 Elements H-Pu. *J. Chem. Phys.* 132, 154104 (2010).
25. S.L. Dudarev, G.A. Botton, S.Y. Savrasov, C. Humphreys, and A.P. Sutton, Electron-Energy-Loss Spectra and the Structural Stability of Nickel Oxide: An LSDA+U Study. *Phys. Rev. B* 57, 1505 (1998).
26. X. Gonze and C. Lee, Dynamical Matrices, Born Effective Charges, Dielectric Permittivity Tensors, and Interatomic Force Constants from Density-Functional Perturbation Theory. *Phys. Rev. B* 55, 10355 (1997).
27. C.D. Brunetta, B. Karuppannan, K.A. Rosmus, and J.A. Aitken, The Crystal and Electronic Band Structure of the Diamond-Like Semiconductor Ag_2ZnSiS_4. *J. Alloy. Compd.* 516, 65 (2012).
28. D. Liu, D. Han, M. Huang, X. Zhang, T. Zhang, C. Dai, and S. Chen, Theoretical Study on the Kesterite Solar Cells Based on $Cu_2ZnSn(S, Se_)4$ and Related Photovoltaic Semiconductors. *Chin. Phys. B* 27, 018806 (2018).
29. S. Chen, X. Gong, A. Walsh, and S.-H. Wei, Defect Physics of the Kesterite Thin-Film Solar Cell Absorber Cu_2ZnSnS_4. *Appl. Phys. Lett.* 96, 021902 (2010).
30. J.-P. Poirier and A. Tarantola, A logarithmic equation of state. *Phys. Earth Planet. Inter.* 109, 1 (1998).
31. T. Nouri, F. Khelfaoui, Y. Benallou, H. Lakhdari, K. Amara, H. Boutaleb, and M. Dahmani, Theoretical Design of Novel Half-Metallic Alloys XMg_3O_4(X = Li, Na, K, Rb). *Appl. Phys. A* 127, 1 (2021).
32. D. Connétable and O. Thomas, First-Principles Study of the Structural, Electronic, Vibrational, and Elastic Properties of Orthorhombic NiSi. *Phys. Rev. B* 79, 094101 (2009).
33. E. Deligoz and H. Ozisik, Mechanical and Dynamical Stability of TiAsTe Compound from ab Initio Calculations. *Phil. Mag.* 95, 2294 (2015).
34. W. Voight, Lehrbuch der Kristallphysik. 1966th edn. (Vieweg+Teubner Verlag).
35. A. Reuß, Berechnung der Fließgrenze von Mischkristallen auf Grund der Plastizitätsbedingung für Einkristalle. *ZAMM-J. Appl. Math. Mech./Zeitschrift für Angewandte Mathematik und Mechanik* 9, 49 (1929).
36. R. Hill, The Elastic Behaviour of a Crystalline Aggregate. *Proc. Phys. Soc. Sect. A* 65, 349 (1952).
37. J.P. Watt, G.F. Davies, and R.J. O'Connell, The Elastic Properties of Composite Materials. *Rev. Geophys.* 14, 541 (1976).
38. L. D. Landau, E. M. Lifšic, E. M. Lifshitz, A. M. Kosevich, L. P. Pitaevskii, *Theory of Elasticity: Volume 7,* 3rd edn. (Elsevier, 1986).
39. H.A. Badehian, H. Salehi, and M. Ghoohestani, First-Principles Study of Elastic, Structural, Electronic, Thermodynamical, and Optical Properties of Yttria (Y_2O_3) Ceramic in Cubic Phase. *J. Am. Ceram. Soc.* 96, 1832 (2013).
40. F. Mouhat and F.-X. Coudert, Necessary and Sufficient Elastic Stability Conditions in Various Crystal Systems. *Phys. Rev. B* 90, 224104 (2014).
41. B. Bekki, K. Amara, and M. El Keurti, First-Principles Study of the New Potential Photovoltaic Absorber: Cu_2MgSnS_4 Compound. *Chin. Phys. B* 26, 076201 (2017).
42. H.B. Xu, Y.X. Wang, and V. Lo, First-Principles Study of CrB4 as a High Shear Modulus Compound. *Physica Status Solidi (RRL)–Rapid Res. Lett.* 5, 13 (2011).
43. K. Refson, P.R. Tulip, and S.J. Clark, Variational Density-Functional Perturbation Theory for Dielectrics and Lattice Dynamics. *Phys. Rev. B* 73, 155114 (2006).
44. S. Baroni, S. De Gironcoli, A. Dal Corso, and P. Giannozzi, Phonons and Related Crystal Properties from Density-Functional Perturbation Theory. *Rev. Mod. Phys.* 73, 515 (2001).
45. H. Levämäki and L. Vitos, Electron Localization Function Implementation in the Exact Muffin-Tin Orbitals Method. *Phys. Rev. B* 103, 035118 (2021).
46. A. Natik, Y. Abid, R. Moubah, F. Khelfaoui, E. Hlil, H. Zaari, A. Benyoussef, M. Abid, and H. Lassri, Structural, Elastic, Electronic and Optical Properties of RbPbI3 Perovskites Studied Using ab-Initio Calculations. *Phase Transit.* 93, 54 (2020).
47. F. Wooten, Optical Properties of Solids. *Am. J. Phys.* 41, 939 (1973).
48. S. Alnujaim, A. Bouhemadou, A. Bedjaoui, S. Bin-Omran, Y. Al-Douri, R. Khenata, and S. Maabed, *Ab initio* Prediction of the Elastic, Electronic and Optical Properties of a New Family of Diamond-Like Semiconductors, Li_2HgMS_4 (M = Si, Ge and Sn). *J. Alloy. Compd.* 843, 155991 (2020).
49. H. Joshi, D. Rai, K. Verma, K. Bhamu, and R. Thapa, Thermoelectric Properties of Tetragonal HALF-HEUSLER COMPOUNDS, TiXSb (X = Ge, Si): A probe from Density Functional Theory (DFT). *J. Alloys Compd.* 726, 1155 (2017).
50. D.J. Singh, Chapter 5 Theoretical and Computational Approaches for Identifying and Optimizing novel Thermoelectric Materials. *Semicond. Semimet.* 70, 125 (2001).
51. R. Woods-Robinson, Y. Han, H. Zhang, T. Ablekim, I. Khan, K.A. Persson, and A. Zakutayev, Wide Band Gap Chalcogenide Semiconductors. *Chem. Rev.* 120, 4007 (2020).
52. Y. Yu, M. Cagnoni, O. Cojocaru-Mirédin, and M. Wuttig, *Adv. Func. Mater.* 30, 1904862 (2020).
53. M. Ali, M.A. Hossain, M. Rayhan, M. Hossain, M. Uddin, M. Roknuzzaman, K. Ostrikov, A. Islam, and S. Naqib, Chalcogenide Thermoelectrics Empowered by an Unconventional Bonding Mechanism. *J. Alloy. Compd.* 781, 37 (2019).
54. Z. Li, W. Zhang, B. Gu, C. Zhao, B. Ye, C. Xiao, and Y. Xie, Vacancy Cluster-Induced Local Disordered Structure for the Enhancement of Thermoelectric Property in Cu 2 ZnSnSe 4. *Journal of Materials Chemistry A*. 9(2), 1006 (2021).
55. A. A. Ahmad, A. Migdadi, A. M. Alsaad, I. Qattan, Q. M. Al-Bataineh, A. Telfah, Computational and experimental characterizations of annealed cu2znsns4 thin film. Heliyon. 8. e08683. (2022).